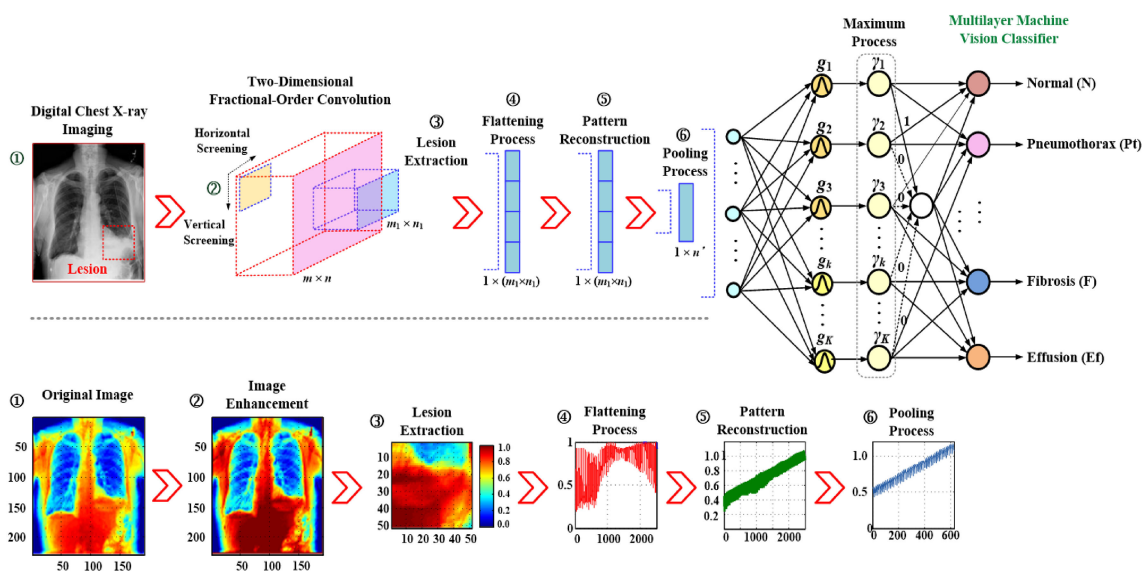🔓Open Access

Enhancement of Chest X-Ray Images to Improve Screening Accuracy Rate Using Iterated Function System and Multilayer Fractional-Order Machine Learning Classifier

Volume 12, Number 4, August 2020

Chia-Hung Lin
Jian-Xing Wu
Chien-Ming Li
Pi-Yun Chen
Neng-Sheng Pai
Ying-Che Kuo

Enhancement of Chest X-Ray Images to Improve Screening Accuracy Rate Using Iterated Function System and Multilayer Fractional-Order Machine Learning Classifier

Chia-Hung Lin [1,2] **Jian-Xing Wu**,[1] **Chien-Ming Li**,[3]
Pi-Yun Chen,[1] **Neng-Sheng Pai**,[1] **and Ying-Che Kuo**[1]

Department of Electrical Engineering, National Chin-Yi University of Technology, Taichung 41170, Taiwan
Artificial Intelligence Application Research Center, National Chin-Yi University of Technology, Taichung 41170, Taiwan
Division of Infectious Diseases, Department of Medicine of Chi Mei Medical Center, Tainan 710, Taiwan

Abstract: Chest X-ray (CXR) images are usually used to identify the causes of patients' symptoms, including the classes of lung or heart disorders. In visualization examination, CXR imaging in anterior–posterior (A–P) views is a preliminary screening method used by clinicians or radiologists to diagnose possible lung abnormalities, such as pneumothorax (Pt), emphysema (E), infiltration (In), lung cancer (M), pneumonia (P), pulmonary fibrosis (F), and pleural effusion (Ef). However, the identification of the causes of multiple abnormalities associated with coexisting conditions presents a challenge. In ruling out a suspected lung disease, the signs and symptoms of physical conditions need to be identified to arrive at a definitive diagnosis. In addition, low contrast CXR images and manual inspection restrict automated screening applications. Hence, this study aims to propose an iterated function system (IFS) and a multilayer fractional-order machine learning classifier to rapidly screen the possible classes of lung diseases within regions of interest on CXR images and to improve screening accuracy. For digital image processes, a two-dimensional (2D) fractional-order convolution is used to enhance symptomatic features. The IFS with nonlinear interpolation functions is then used to reconstruct the 2D feature patterns. These reconstructed patterns are self-affine in the same class and thus help distinguish normal subjects from those with lung diseases. The accuracy rate is thus improved. Pooling is performed to reduce the dimensions of the feature patterns and speed up complex computations. A gray relational analysis-based classifier is used to identify the possible classes of the signs and symptoms of lung diseases. For digital CXR images in A-P view, the proposed multilayer machine learning classifier with k-fold cross-validation presents promising results in screening lung diseases and improving screening accuracy rate relative to traditional methods. The proposed classifier is evaluated in terms of recall (99.6%), precision (87.78%), accuracy (88.88%), and F1 score (0.9334).

Index Terms: Chest X-ray, iterated function system, multilayer machine-learning decision-making classifier, fractional-order convolution, nonlinear interpolation function.

1. Introduction

Lung diseases may refer to several types of diseases or disorders that affect the pulmonary functions in one or both sides of lungs and the right/left upper, middle, or lower lung regions; they are caused by influenza, infection, tuberculosis, pulmonary edema, aspiration pneumonia (AP), and lung cancer, which can lead to breathing problems or acute respiratory distress syndrome (ARDS). Smoking is the most common cause of respiratory diseases and a common risk for lung cancer. The incidence of this case has increased in about 25% of lung cancers patients who are never-smokers [1], [2]. Several lung diseases, such as asthma and lung cancer, are caused by environmental factors. Asthma symptoms include a chronic respiratory condition with difficulty in breathing due to airway inflammation, allergies, or pollution. Asthma is a reversible obstructive lung disease. Subjects with asthma have improved breathing flow rates compared with those with chronic obstructive pulmonary disease (COPD). COPD, emphysema (E), and chronic bronchitis are serious respiratory diseases and associated with cigarette smoking; they reduce air flow and cause difficulty in breathing. Acute bronchitis is the sudden infection of the airways caused by a virus. The above diseases all affect the airways.

Lung diseases affect the alveolus; these diseases include pneumonia (P), tuberculosis, pulmonary edema, lung cancer, and ARDS. P presents with lung infection and infiltration symptoms, such as those of the novel coronavirus disease (COVID-19), severe acute respiratory syndrome (SARS), ARDS, AP, and influenza [3]–[6]; these conditions are caused by bacterial, viral, or fungal infections, as shown in Fig. 1. P causes inflammation of the alveolus, resulting in filling of the lungs with fluid or pus and reduced ability to hold air. The death rate of P is high in Taiwan, ranking third after cancer and heart diseases and accounting for 13.4 thousand deaths [males (68.3%) higher than females (45.7%)] in 2019 [7]. A high risk was also observed among individuals older than 65 years, type 2 diabetes mellitus, and cardiovascular diseases. Pulmonary infiltration (In) is caused by P, tuberculosis, and nocardiosis; it results in the accumulation of abnormal substances, such as pus, blood, or protein, within cells or body tissues or spreads through the interstices of the lung [8]. In addition, lung diseases of the pleura include pleural effusion (Ef) and pneumothorax (Pt). Ef is caused by heart failure, P, pulmonary hypertension, malignancy, and chest surgery. Large pleural Ef size ($>$1,000 mL) [9], [10] will affect the breathing, and Ef should be drained. Pt may occur in COPD for about 70% of these cases [11], [12]. The above lung diseases can be diagnosed using visualization examination with the upright chest X-ray (CXR) in anterior–posterior (A-P) or lateral view, chest computed tomography (CT) scan, and chest ultrasound [4], [9]–[10], [13]–[15]. In visualization examination, a CXR has A-P or lateral view for bilateral lung imaging in a standing position, which can be digitalized to apply for the rapid detection of abnormalities using artificial intelligent methods [4], [16]–[18]. CXR can also be used to observe the disease progression during hospital admission. For example, in the *Streptococcus pneumoniae* pneumonia presented in Fig. 2, the subject (gender: female, age: 25 years) showed an opacity spreading to the right upper lung lobe and a developing opacity in the left lung (LL) [marked by the bounding box with a blue dashed line in Figs. 2(b) and 2(c)]. This result is consistent with the widespread infection in the right and left regions from Day 0 to Day 3. The right heart border was not observed. The original CXR images can be enhanced to clearly to point out the opacity regions resulting from infection and effusion in the right and left lungs [bounding boxes in Fig. 2(c)]. Hence, CXR images can inform physicians about appropriate treatments and help them rule out any suspected lung disease.

When any lung disease gradually develops, the lung becomes inflamed and stiff, preventing the alveoli from fully expanding to limit the oxygen exchange. Upright CXR imaging is a rapid method to screen various lung conditions. Through CXR image inspection, any lesion may appear as white portions in the right/left chest cavity, and air spaces appear as black portions, as shown in Figs. 1 and 2, respectively. Hence, digital CXR images can be used to directly identify and locate the lesions in A-P or lateral views. However, manual inspection has limitations: (1) poor-quality CXR images need to be enhanced to view the contents within the chest cavity; (2) diagnostic results depend on clinicians'/radiologists' interpretations and experiences; (3) considerable time is needed
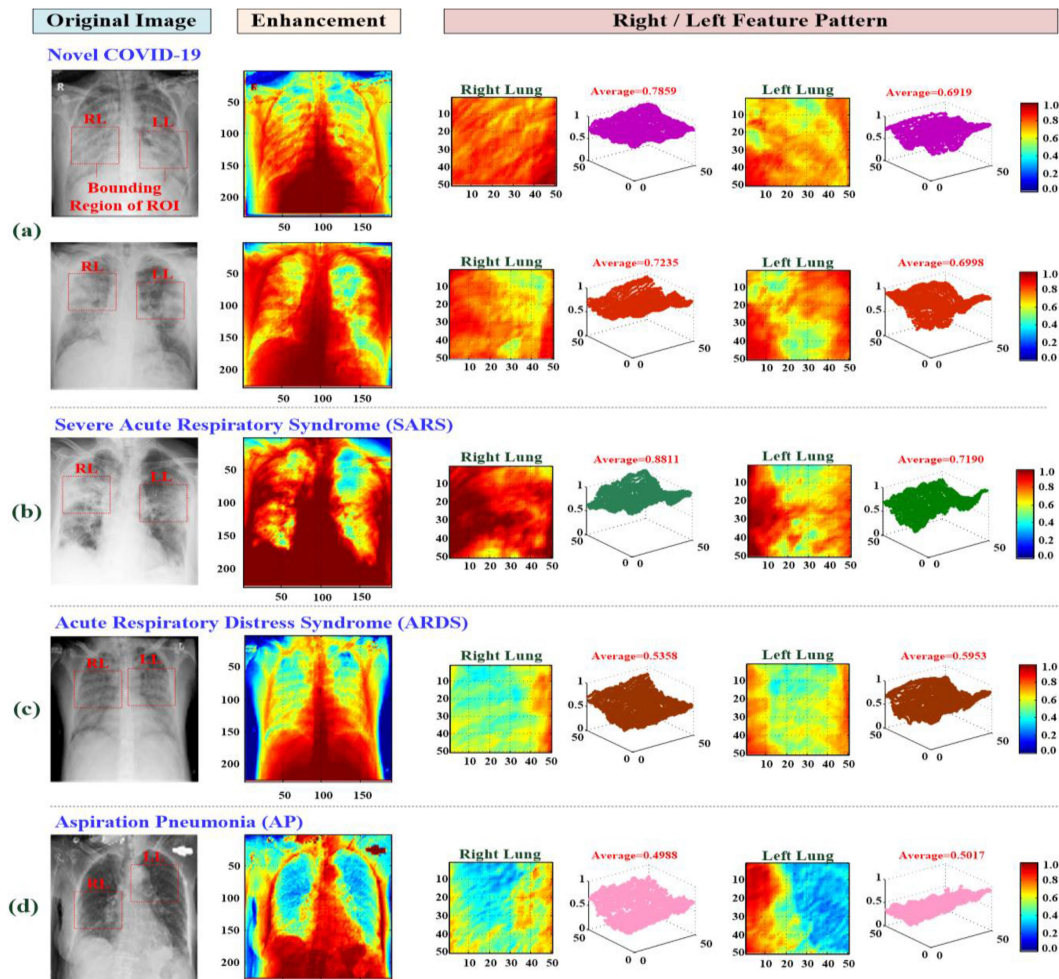
Fig. 1. Original X-ray image, image enhancement, and right/left feature patterns with 2D FOC operation for pneumonia (P) with lung infection and infiltration. (a) Novel COVID-19, (b) SARS, (c) ARDS, (d) AP.

for identifying single and multi classes for any amount of CXB images. Thus, in this study, a two-dimensional (2D) fractional-order convolution (FOC) operation (with appropriate fractional-order parameters, $0.0 < v < 1.0$) [19], [20] in horizontal and vertical directions is applied to enhance images or detect edges within a bounding region of interest (ROI) (right/left feature patterns in Fig. 1). This operation can remove noise, sharpen specific features, or brighten an image so as to easily detect pixel value changes and identify changes in the right / left lung tissues [21]. This spatial domain-based convolution operation can preserve high-frequency contour features and improve low-frequency texture details in a smoothing region, and it does not introduce noise during image enhancement [10], [20].

In real world, fractals reconstructing patterns can be produced by the iteration of one or more affine transformations (ATs) which can yield a new attractor in the final image. With a finite set of ATs, we can reconstruct a new feature pattern using several ATs, with each AT having a 2×2 transformation matrix and a 2×1 translational vector, the so-called "Iterated Function System (IFS)" [21]–[24]. Hence, in this study, Katz's algorithm [24], [25] is used to estimate fractal dimension (FD) with finite sampling data. After the enhancement of CXR images with the 2D FOC operation, specific features on the bounding ROI can be sharpened and brightened. The IFS with nonlinear interpolation functions (NIFs) is proposed to model affine maps for reconstructing feature patterns,
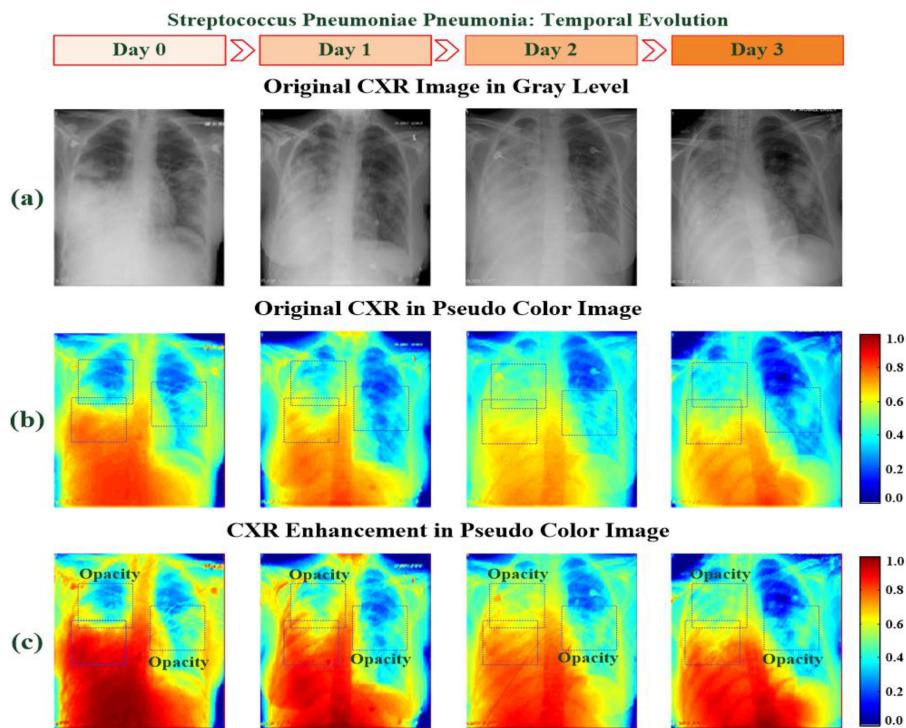
Fig. 2. Progression of CXR images during hospital admission (Day #0 - #3) for *streptococcus pneumoniae pneumonia* in frontal view. (a) Original CXR images in Gray level, (b) Original CXR in pseudo color image, (c) CXR enhancement in pseudo color image.

including eight classes: normal (N) control, Pt, E, In, M, P, F, and Ef. The IFS model can produce various fractal feature patterns in vector forms. Hence, after image enhancement and feature extraction with a specific bounding box (B-box), the new feature pattern can be reconstructed in the higher dimensional feature space and lead to separability in the feature space to improve the screening accuracy in nonlinear separable classification or in multilabel image classification problems. Then, a gray relational analysis (GRA) [26]–[29] based on a multilayer machine vision classifier is carried out to deal with nonlinear separable tasks for multiclass classification to distinguish the N control from those with lung diseases. In the validation stage, A-P CXR images from the National Institutes of Health (NIH) CXR database (NIH Clinical Center) are enrolled [30]. The K-fold cross- validation is used to verify the performance of the proposed multilayer machine vision classifier with recall (%), precision (%), accuracy (%), and F1 score [31].

The remainder of this article is organized as follows: Section II describes the methodology for multilabel image classification problems, including the experimental setup, image enhancement with 2D FOC process, feature pattern reconstruction of the IFS, and GRA-based multilayer classifier design. Sections III and IV present the experimental results and discussion, respectively, in comparison with the traditional multilayer neural network and the conclusion.

2. Methodology

2.1 Experimental Setup

The NIH Clinical Center has released private CXR images from more than 30,000 patients for scientific research; the images consisted of A-P view CXR images with labeled lung and cardiac-related diseases [4], [16]–[18], [30]. These images with labeled classes will allow scientific researchers to analyze the diseases affecting the airways, alveoli, interstitium, pleura, and blood vessels. Through

TABLE 1
The Profile of the Enrolled Subjects [30]

Aged Range	Female (F)	Male (M)
$0 - 30$ (43)	22.14 ± 6.78 (21)	20.50 ± 6.31 (22)
$30 - 60$ (168)	47.45 ± 7.72 (80)	46.25 ± 8.13 (88)
$60 - 90$ (59)	68.74 ± 6.01 (19)	70.15 ± 6.42 (40)
$0 - 90$ (270)	46.55 ± 15.21 (120)	48.84 ± 17.35 (150)

clinical research, physicians or clinician investigators can translate research results into better therapies, treatments, and interventions in clinical trials. However, patients may have single or multiple symptoms, which will cause difficulty in localization of pathologies. Therefore, a computer-aided decision-making (CADM) tool must be designed for the multi-label image classification problems.

These collected images with labeled classes allow clinical and engineering researchers to analyze the datasets for designing the CADM tool. In lectures [4], [16]–[18], [32]–[37], digital image process, statistical, multilayer machine learning, and deep learning methods have been applied to various machine vision classifiers for automatic lung and cardia-related disease classifications, such as Haar features, histogram of oriented gradients features, rule-based image segmentation [32]–[36], linear discriminators, multilayer neural networks, deep learning neural networks, support vector machines, and so on [4], [16]–[18], [37]–[40]. In multilayer classifiers, supervised backpropagation or unsupervised competitive-based learning algorithms are used to train the multilayer neural networks or deep learning neural networks. However, these methods require the assignment of the network connecting weights in multi-hidden layers by using iteration computations, which will increase the rate of design cycle

The GRA algorithm [26]–[29] was used to design a classifier to identify the multi label classes in the right lung (RL) and LL. The model consists of a radial Bayesian network (RBN) with Gaussian activation functions, gray relational pattern analysis with Euclidean distance (ED), and maximum and minimum operations, which are straightforward mathematical operations for nonlinear mapping of the EDs to the degrees of similarity between the training and untraining patterns; thus, regardless of the ED, the range of relational grade, as gray grade (GG), can be bounded in a specific closed range [0, 1]. A recognition coefficient will enhance the distinguishing relational grade in *GG*. Therefore, by feeding the clinical dataset through an ongoing investigation, artificial intelligence-based CADM method can gradually refine diagnostic precision in clinical applications. In this study, 270 subjects aged 1–89 years (mean age: 47.82 ± 16.22 years), including 120 females (mean age: 46.55 ± 15.21 years) and 150 males (mean age: 48.84 ± 17.35 years), are selected for validation of the proposed classifier (as seen in Table 1) [30], [41]. CXR images are collected from the 270 subjects and converted into a tagged image file format. Each image is digitized to a resolution of 96×96 dots per inch, thereby producing 24 bits per pixel which are then incorporated into a 190×230 pixel image (43,700 pixels). Spatial domain-based convolution with fractional-order mask is used to enhance the images on bounding ROIs. Then, the right and left feature patterns are extracted with a specific 50×50 B-box from different subjects with single or multiple lung-related diseases. The dataset was based on feature patterns, which can be divided into two groups of dataset: one group (trained patterns) for training the classifier in training stage and the remaining feature patterns (untrained patterns) for testing the classifier in each fold cross-validation in recalling stage. The performance is evaluated by recall (%), precision (%), accuracy (%), and F1 score indices.

2.2 Image Enhancement With 2D Fraction-Order Convolution Process

Fractional-order multi-scale convolution process has been designed for digital signal process and image (texture) enhancement. This process can be used to enhance specific features (possible abnormalities) in both LL and RL in a digitized CXR image, offering a gray gradient-based feature patterns to solve the classification and contour search [10], [34]–[35], [38] for identifying and

(a) $\begin{bmatrix} 0 & \frac{v^2-v}{2} & 0 \\ 0 & -v & 0 \\ 0 & 1 & 0 \end{bmatrix}$
(b) $\begin{bmatrix} 0 & 0 & \frac{v^2-v}{2} \\ 0 & -v & 0 \\ 1 & 0 & 0 \end{bmatrix}$
(c) $\begin{bmatrix} 0 & 0 & 0 \\ 1 & -v & \frac{v^2-v}{2} \\ 0 & 0 & 0 \end{bmatrix}$
(d) $\begin{bmatrix} 1 & 0 & 0 \\ 0 & -v & 0 \\ 0 & 0 & \frac{v^2-v}{2} \end{bmatrix}$
(e) $\begin{bmatrix} 0 & 1 & 0 \\ 0 & -v & 0 \\ 0 & \frac{v^2-v}{2} & 0 \end{bmatrix}$
(f) $\begin{bmatrix} 0 & 0 & 1 \\ 0 & -v & 0 \\ \frac{v^2-v}{2} & 0 & 0 \end{bmatrix}$
(g) $\begin{bmatrix} 0 & 0 & 0 \\ \frac{v^2-v}{2} & -v & 1 \\ 0 & 0 & 0 \end{bmatrix}$
(h) $\begin{bmatrix} \frac{v^2-v}{2} & 0 & 0 \\ 0 & -v & 0 \\ 0 & 0 & 1 \end{bmatrix}$

Fig. 3. Eight fractional-order operators in eight directions. (a) negative x-coordinate, (b) right upward diagonal, (c) positive y-coordinate, (d) right downward diagonal, (e) positive x-coordinate, (f) left downward diagonal, (g) negative y-coordinate, (h) left upward diagonal.

locating the lesions. A fractional-order operator has multiple symmetric directions and can rotate clockwise every 45° in eight directions, as seen 8 fractional- order operators in Figs. 3(a) to 3(h), including negative x-coordinate, right upward diagonal, positive y-coordinate, right downward diagonal, positive x-coordinate, left downward diagonal, negative y-coordinate, and left upward diagonal directions, respectively. A multiscale general form with a Grümwald–Letnikov fractional-order differentiator [19] for signal process can be expressed as follows:

$$\frac{d^v s(t)}{dt^v} \cong \frac{t^{-v} n^v}{\Gamma(-v)} \sum_{k=0}^{n-1} \frac{\Gamma(k-v)}{\Gamma(k+1)} s\left(t - \frac{kt}{n}\right) \tag{1}$$

where $s(t)$ is the time-varying signal in a 1D signal; v is the fractional-order parameter, $0 < v < 1$, $v \in R$; $\Gamma(\bullet)$ is the gamma function; and n is the finite number of nonzero terms. The general fractional-order form is a polynomial function determined as the sum of nonzero terms. For a 2D digitized CXR image processing, Equation (1) can be modified and be proximately expressed in horizontal (x) and vertical (y) directions by simplifying the fractional-order differentiator [19]:

$$\frac{d^v I(x, y)}{dx^v} \cong a_0 I(x, y) + a_1 I(x-1, y) + a_2 I(x-2, y) + a_3 I(x-3, y) + \cdots + a_{n-1} I(x-n+1, y) \tag{2}$$

$$\frac{d^v I(x, y)}{dy^v} \cong a_0 I(x, y) + a_1 I(x, y-1) + a_2 I(x, y-2) + a_3 I(x, y-3) + \cdots + a_{n-1} I(x, y-n+1) \tag{3}$$

where $I(x, y)$ is the pixel value at location (x, y) in a CXR image, $I(x, y) \in [0, 255]$; $x = 1, 2, 3, \ldots, W$, and $y = 1, 2, 3, \ldots, H$, in which W and H are the image width and height, respectively; parameters $a_0, a_1, a_2, a_3, \ldots, a_{n-1}$, and a_n are the polynomial coefficients and can be expressed respectively as [19]

$$a_0 = 1, \quad a_1 = (-v), \quad a_2 = \frac{(-v)(-v+1)}{2}, \quad a_3 = \frac{(-v)(-v+1)(-v+2)}{2}, \ldots,$$

$$a_k = \frac{\Gamma(k-v)}{(k)!\Gamma(-v)}, \cdots, a_{n-1} = \frac{\Gamma(n-v-1)}{(n-1)!\Gamma(-v)}, \quad a_n = \frac{\Gamma(n-v)}{n!\Gamma(-v)} \tag{4}$$

These polynomial coefficients can be used to set the elements of fractional-order operator, as seen in Fig. 3, where $k \to n = 2m - 2$, the dimension of fractional-order mask, $(2m - 1) \times (2m - 1)$, can be designed, and n should be an even finite number ($n = 2, 4, 6, \ldots$) to ensure that the fractional-order mask has a specific center. Hence, a 3×3, 5×5, $\ldots$, or $(2m - 1) \times (2m - 1)$ fractional-order mask, $m = 2, 3, 4, \ldots$, can be designed for the local convolution process. In this study, the size of $m = 2$ is selected to construct 3×3 mask matrices. Then, two fractional-order operators with three coefficients, a_0, a_1, and a_2 (as a_1 be a center in a mask matrix), can be implemented in both horizontal (x) and vertical (y) directions:

$$M_x = \begin{bmatrix} 0 & a_2 & 0 \\ 0 & \boxed{a_1} & 0 \\ 0 & a_0 & 0 \end{bmatrix}, \quad M_y = M_x^T = \begin{bmatrix} 0 & 0 & 0 \\ a_2 & \boxed{a_1} & a_0 \\ 0 & 0 & 0 \end{bmatrix} \tag{5}$$

where M_x and M_y are shown in Fig. 3(a) (negative x-coordinate) and Fig. 3(g) (negative y-coordinate), respectively. For digital CXR imaging, the spatial domain-based fractional-order operators are used to enhance the CXR images by convolving the horizontal and vertical directions [10]:

$$G_x^v I(x, y) = \sum_{i=-\frac{h-1}{2}}^{\frac{h-1}{2}} \sum_{j=-\frac{h-1}{2}}^{\frac{h-1}{2}} M_x(i, j) I(x + i, y + j) \tag{6}$$

$$G_y^v I(x, y) = \sum_{j=-\frac{h-1}{2}}^{\frac{h-1}{2}} \sum_{i=-\frac{h-1}{2}}^{\frac{h-1}{2}} M_y(j, i) I(x + j, y + i) \tag{7}$$

where $h = 3$ is the size of the mask matrix for the 3×3 fractional-order operator; and i and j are the row and column numbers in the mask matrix, respectively. The fractional-order gradient can be computed and normalized as follows [10]:

$$\nabla^v I(x, y) = \sqrt{(G_x^v I)^2 + (G_y^v I)^2} \cong |G_x^v I| + |G_y^v I| \tag{8}$$

$$\nabla I = \frac{|G_x^v I| + |G_y^v I|}{255}, \tag{9}$$

where ∇I is the normalized gray gradient, $\nabla I \in [0, 2]$. With the simplified forms, $|G_x^v I|$ and $|G_y^v I|$, each convolution computation involves row and column elements, $M_x(i, j) = M_y(j, i)$. Each element is multiplied by the corresponding input discrete pixel values, $I(x, y)$, $x = 1, 2, 3, \ldots, W$, and $y = 1, 2, 3, \ldots, H$, which are used to enhance CXR images via convolution with structure tensor masks M_x and M_y.

2.3 Feature Patterns Reconstruction

An IFS [21–24] is a model to reconstruct the feature pattern as stream data by NIFs, which can perform family functions with different FDs. Its model is a finite set of mapping functions for interpreting the sampling data to be modeled as a self-similarity pattern. Given a data sequence from the flattening process layer, $\Phi = [\nabla I_1, \nabla I_2, \nabla I_3, \cdot, \nabla I_i, \cdot, \nabla I_N]$, $i = 1, 2, 3, \ldots, 2,500$ ($W = 50$, $H = 50$, and $N = 2,500$ in this study), $\nabla I_i \in [0, 2]$, the pth interpolation map, Φ_p, $p = 1, 2, 3, \ldots, N$, can be presented in matrix form using IFS:

$$\Phi_p\left(\begin{bmatrix} i \\ \nabla I_i \end{bmatrix}\right) = \begin{bmatrix} a_i & b_i \\ c_i & d_i \end{bmatrix} \begin{bmatrix} i \\ \nabla I_i \end{bmatrix} + \begin{bmatrix} e_i \\ f_i \end{bmatrix} \tag{10}$$

For a flattening pattern in a vector form, Equation (1) can be represented as follows:

$$\Phi_p(i) = a_i i + b_i \nabla I_i + e_i \tag{11}$$

$$\Phi_p(\nabla I_i) = c_i i + d_i \nabla I_i + f_i, \tag{12}$$

where parameters, $b_i = e_i = f_i$, are set to zero, and the parameter, $a_i = 1$, is fixed; the function $\Phi_p(i) = i$ will become a linear interpolation function. For reconstructing the feature pattern, function $\Phi_p(\nabla I_i)$ as a NIF can map the stream data onto a reconstructed feature pattern with n interpolation
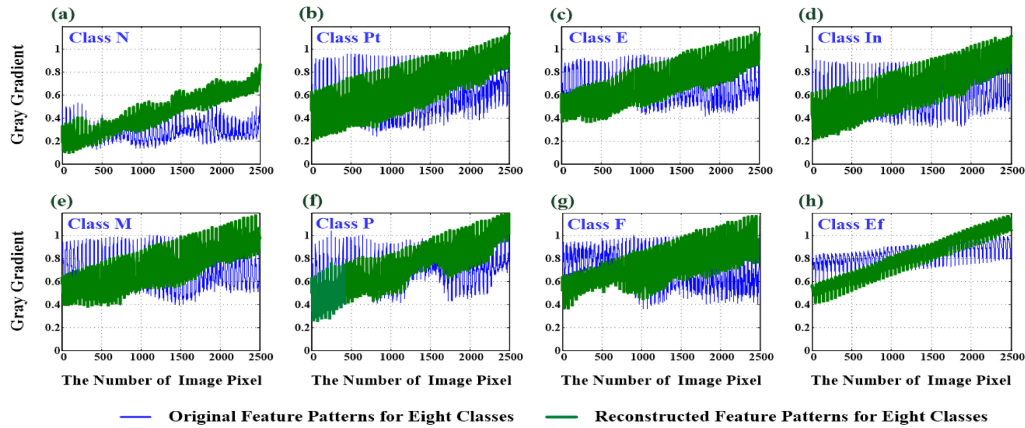
Fig. 4. Original feature patterns and reconstructed feature patterns for eight classes. (a) N, (b) Pt, (c) E, (d) In, (e) M, (f) P, (g) F, (h) and Ef.

Note: (1) N: 1-25; (2) Pt: 26-59; (3) E: 60-74; (4) In: No. 75-102; (5) M: No. 103-127; (6) P: No. 128-173; (7) F: No. 174-198; (8) Ef: No. 199-223
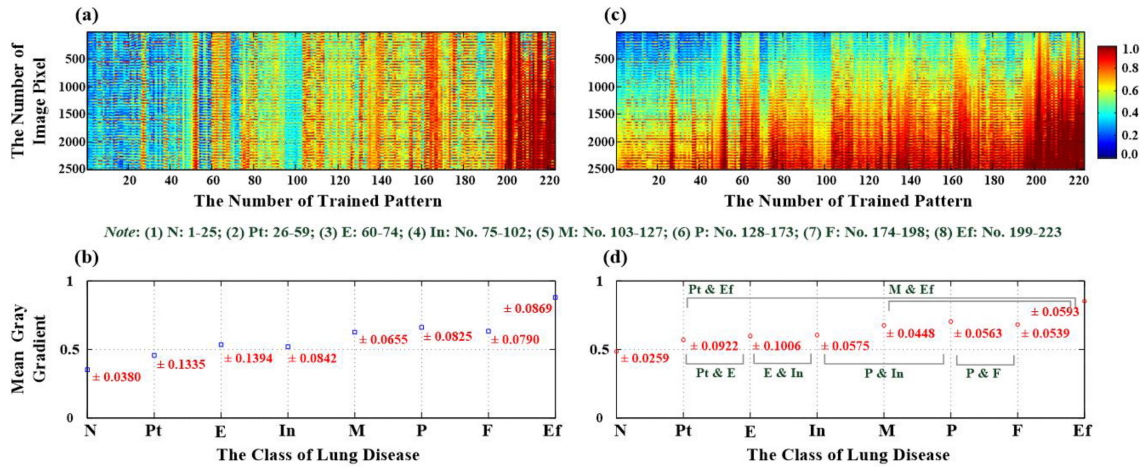
Fig. 5. Feature patterns and mean gray gradients versus classes of lung diseases. (a) The 223 feature patterns for eight classes, (b) 223 feature patterns with fractal interpolation reconstruction for eight classes, (c) mean gray gradients versus classes of lung diseases, and (d) mean gray gradients versus classes of lung diseases with fractal interpolation reconstruction.

points, and a reconstructed pattern can be created point by point as follow:

$$\Phi_p(\nabla l_i) = c_i \Phi_p(i) + d_i \nabla l_i \tag{13}$$

$$\Phi_p(i) = \frac{1}{2} \, \text{mod} \, (\Phi_p(\nabla l_i), N') \tag{14}$$

where parameters $c_i = \frac{1}{N}$ and $d_i = D = \frac{\log_{10}(N')}{\log_{10}(N)}$; D is the FD, $D \in (1, 2)$ for all feature patterns, $0 < N < N'$, $N' = 190 \times 230$ (43,700) is the number of CXR image pixel, $N = 50 \times 50$ (2,500) is the number of B-box pixel, $d_i = D = 1.3657$ in this study, and mod(•) is the modulo operator. FD can be estimated by Katz's algorithm [24], [25]. Equation, $\Phi_p(i)$, $i = 1, 2, 3, \cdot, N$, $\Phi_p(i) \in [0, 2]$, is a simple form to reconstruct the complicated pattern. The fractal interpolation method as Equations (13) and (14) is carried out to reconstruct the feature patterns with the data samples, and the resulting reconstructed feature patterns are self-affine in the same class, including normal (N) condition (25), Pt (34), E (15), In (28), M (25), P (46), F (25), and Ef (25), as seen in Fig. 4.

For example, given 223 feature patterns for eight classes (Fig. 5(a)), the reconstructed feature patterns were created using Equations (13) and (14), as shown in Fig. 5(c)). The statistics for
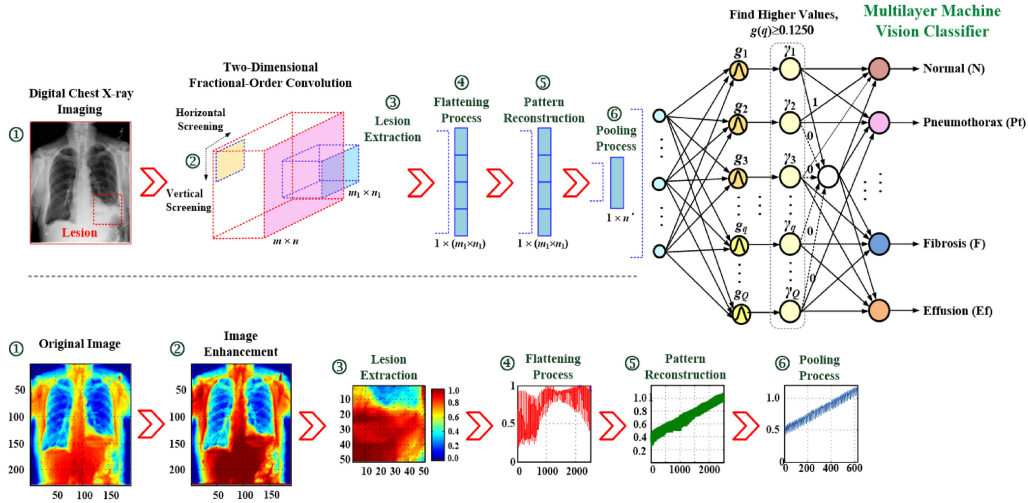
Fig. 6. Multilayer machine vision classifier for typical lung disease screening, including image enhancement process, lesion extraction with B-box, flattening process, pattern reconstruction, pooling process, and pattern recognition.

mean gray gradients and their standard deviations were obtained using the 223 feature patterns, as shown in Figs. 5(b) and 5(d). The correlation between the mean gray gradients and symptom classes indicates that the changes of gray gradients in a linear regression curve ($R^2 = 0.8552$) with a positive correlation between the mean gray gradients and eight classes. The correlation could be used to quantify the gray gradient's feature patterns to identify the possible classes. In Fig. 5(d), feature patterns are recreated by fractal interpolation in gray gradient, and reconstructed feature patterns of eight classes, including single class (N, Pt, E, In, M, P, F, Ef) and multi classes (Pt & E, E & In, P & In, P & F, Pt & Ef, M & Ef), were dispersed in eight regions of the feature space, which rendered the features more distinguishable to aid in classification for separating true positive (TP) from true negative (TN). Then, the multilayer machine vision classifier is used to screen the normal control and lung disease subjects. The next section will introduce the classifier method.

2.4 Multilayer Classifier Design

After feature pattern reconstruction (as presented by symbol "⑤" in Fig. 6), a pooling process is used to decrease the dimension of the feature pattern from $1 \times 2,500$ to 1×625. The pooling feature pattern, $\Psi(i)$, $i = 4\hat{\imath}$, $\hat{\imath} = 0, 1, 2, 3, \ldots, n'\text{-}1$ ($n' = 625$ in this study), is obtained by taking every 4th sample of the feature pattern $\Phi_p(i)$. Then, the pooling feature pattern is fed into the input layer of a GRA-based classifier to perform the pattern recognition tasks, as indicated by the symbol "⑥" in Fig. 6. A GRA method uses the numerical measure of similarity between two sequence data, defining the reference sequence (testing feature pattern), $\Psi_0 = [\phi_1(0), \phi_2(0), \cdot, \phi_i(0), \cdot, \phi_{625}(0)]$, and Q comparative sequences (training feature pattern), $\Psi_q = [\phi_1(q), \phi_2(q), \cdot, \phi_i(q), \cdot, \phi_{625}(q)]$, $q = 1, 2, 3, \ldots, Q$. The output of GRA as GG distributed between zero and one, as a "Gaussian function", can be defined as [28]:

Gray grade (GG):

$$g(q) = \xi \exp\left(-\frac{1}{2}\left(\frac{ED(q)^2}{\sigma^2}\right)\right) \tag{15}$$

Euclidean distance (ED):

$$ED(q) = \sqrt{\sum_{i=1}^{n'} (\Delta d_i(q))^2}, \ \Delta d_i(q) = \nabla\varphi_i(0) - \nabla\varphi_i(q) \tag{16}$$

Variance:

$$\sigma^2 = (\Delta d_{\max} - \Delta d_{\min})^2, \begin{cases} \Delta d_{\min} = \min_{\forall i \forall q}[\Delta d_i(q)] \\ \Delta d_{\max} = \max_{\forall i \forall q}[\Delta d_i(q)] \end{cases} \tag{17}$$

where $\Delta d_{\max}$ and $\Delta d_{\min}$ are the maximum and minimum deviation values, respectively; the standard deviation (σ) is estimated by $(\Delta d_{\max} - \Delta d_{\min})$. In Equation (15), $g(q)$ is used to measure the similarity degree between a reference sequence (testing pattern) and Q comparative sequences (training patterns). $g(q)$ is inversely proportional to the EDs, that is, when $ED \to ED_{\max}$, $g(q) \to 0$, and $ED \to ED_{\min}$, $g(q) \to \xi$; ξ is the recognition coefficient (RC), $\xi \in (0, 5]$. Parameter ξ is used to make the GG clearly distinguishable between pattern Ψ_0 and qth pattern Ψ_q so as to select $\xi \gg 1$ to increase contrast; Q comparative sequences are created by the reconstructed feature patterns, as indicated by the classes N, Pt, E, In, M, P, F, and Ef in Fig. 5(c).

When input reference sequence Ψ_0 is similar to any comparative sequence Ψ_q in Q datasets, the $g(q)$ will reach a higher value, which can be obtained by referring to the criterion index $q*$ as follows:

$$\gamma_q = \begin{cases} 1, & g(q) \geq 0.125, q = q* \\ 0, & q \neq q* \end{cases}, \gamma_q \in [0, 1] \tag{18}$$

where the threshold value of 0.125 is set in screening high values for any possible class. In this study, the associated class for reference sequence Ψ_0 can be encoded as connecting weighed values, $w_{qj} \in [0, 1]$, between Q GG functions and eight classes ($Q \times 8$), that is, $j = 1, 2, 3, \ldots,$ 8, using binary values with a value of "1" denoting a possible class and a "0" value for all other classes. For example, for a single class #N, the weight values, w_{qj}, can be denoted as [N, Pt, E, In, M, P, F, Ef] = [1, 0, 0, 0, 0, 0, 0, 0]; for multiple classes (labels) #P and #F, w_{qj} can also be denoted as [0, 0, 0, 0, 0, 1, 1, 0]. If Ψ_0 belongs to any class, then the final output of the GRA-based classifier can be represented as follows:

$$y_j = \sum_{q=1}^{Q} w_{qj}\gamma_q \bigg/ \sum_{q=1}^{Q} \gamma_q, w_{qj} = \begin{cases} 1, & q \in Class\# j \\ 0, & q \notin Class\# j \end{cases} \tag{19}$$

$$O_j = \begin{cases} 1, & y_j \geq 0.50 \\ 0, & y_j < 0.50 \end{cases}, \tag{20}$$

where the threshold value of 0.5 is set to confirm the *disease present* (value 1) or *disease absent* (value 0); the output vector can be labeled as O = [N, Pt, E, In, M, P, F, Ef] = [o_1, o_2, o_3, o_4, o_5, o_6, o_7, o_8], $o_j \in [0, 1]$. With an openly available CXR image database and ongoing clinical investigation dataset [30], [41], the CRA-based classifier can gradually train and refine diagnostic precision in clinical applications, as shown in the flowchart of the screening procedure in Fig. 7, including the dataset collection and labeling, feature extraction, classifier training and validation in learning and recalling stages, and classifier refinement with new clinical CXR images. Indexes, including recall (%), precision (%), accuracy (%), and F1 score, are used to validate the classifier performance in the recalling stage and clinical validation.

3. Experimental Results and Discussion

In this study, 270 subjects were collected from the CXR database; the subjects included 230 individuals from the NIH CXR database [30] with typical lung diseases (N, Pt, E, In, M, P, F, and Ef) and 40 subjects from COVID-19 CXR database [41] with novel COVID-19 (25), SARS (7), *Streptococcus pneumoniae* pneumonia (5), and ARDS (3). The subjects were classified into (1) female (120 subjects) and (2) male groups (150 subjects) (as seen in Table 1) [30], [41]. Among the subjects, novel COVID-19 indicated several unique features, which were confirmed by using
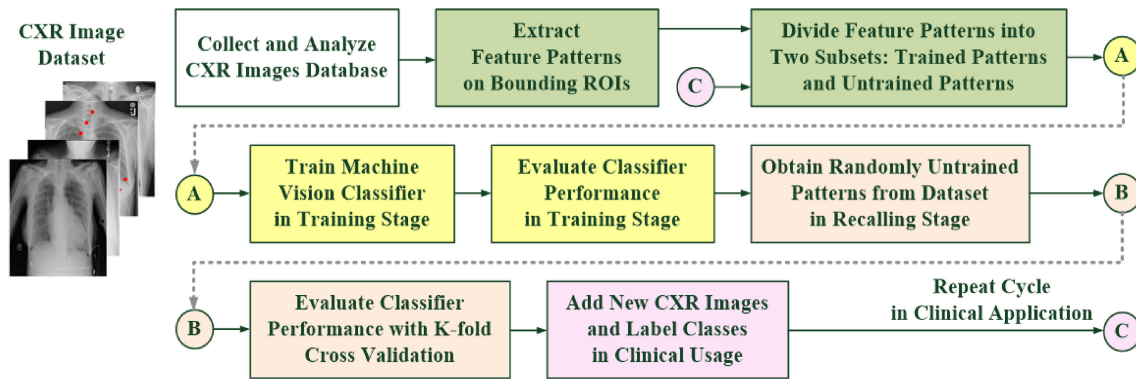
Fig. 7. Flowchart for rapid lung disease screening, including the training stage, recalling stage, and cross-validation.

real-time reverse transcription–polymerase chain reaction (PCR) and conventional PCR method. The infected subjects with P might also present symptoms on CXR and CT images compared with those that had moderate characteristics for reliable identification of a possible case of COVID-19. However, PCR is a general technique for replicating a particular region of DNA, and it is used to match crime scene DNA with suspects. The DNA amplified by PCR might be sent for sequencing, visualized by electrophoresis, or cloned into a plasmid for further experiments, such as biological research, medical diagnostics, or branches of ecology [42]–[44]. This rapid process requires about 45–60 min to complete 40 cycles, depending on the particular protocol and instrument used [45]. Upright CXR imaging is a first-line examination method used to directly inspect and locate any abnormality with bilateral involvements, such as multiple lobular and subsegmental areas of consolidation constitute or In in intensive care unit for novel COVID-19 cases [46]. Hence, CXR images could be used to rapidly screening-related lung diseases.

Feature patterns (446), including 50 Ns, 68 Pts, 30 Es, 56 Ins, 50 Ms, 92 Ps, 50 Fs, and 50 Efs, were captured from all subjects, and they were divided into 223 trained datasets and 223 untrained datasets. Each dataset is a pair of a reconstructed feature pattern (input patterns in Fig. 5(c)) and a label pattern with binary values (output pattern). Each output pattern was encoded with value of 1 or 0 for the eight classes. A value of "1" was given for a possible class associated with the input pattern, and the other values were encoded as "0" using Equation (19). All feature patterns were extracted from the CXR images by using a screenshot–graphical user interface (LabWindows[TM] / CVI[TM], 2019, NI[TM], Austin, TX, USA) and labeled by radiologists as single or multiple classes. In clinical practice, clinicians or radiologists could move the 50×50 B-box (2,500 pixels) to locate and select possible lesions, and each feature pattern could be captured in a screenshot. In image enhancement, the 2D FOC operation with fractional-order parameters, $0.00 < v < 1.00$, was used to enhance the feature patterns (Fig. 8). The feature patterns were over-enhanced with $v < 0.30$ and were decayed with $v > 0.40$. The fractional-order parameters from 0.01 to 0.90 could not totally fit the CXR image enhancement. The appropriate parameters, $v = 0.30$–0.40, could adequately sharpen and brighten the specific features for possible focus on the right or left cavity, as shown in P and F in Figs. 8(a) and 8(b). Hence, these feature patterns could be offered to train and validate the proposed classifier in learning and recalling stages. The proposed multilayer machine vision classifier was implemented on a tablet PC using a high-level programming language in LabVIEW (NI[TM], Austin, TX, USA) and MATLab 9.0 (MathWorks, Natick, MA, USA). These application programs were operated using a graphics processing unit (GPU) on a tablet PC (Intel Xeon, CPU E5-2620, v4, 2.1 GHz and 64 GB of RAM; GPU: NVIDIA Quadro P620, 64-bits Windows 10.0 operating system) to speed up the digital image processing and lung disease screening. Experimental tests indicated the GRA-based classifier's training and testing performances to validate the proposed automated screening methods, as detailed below.
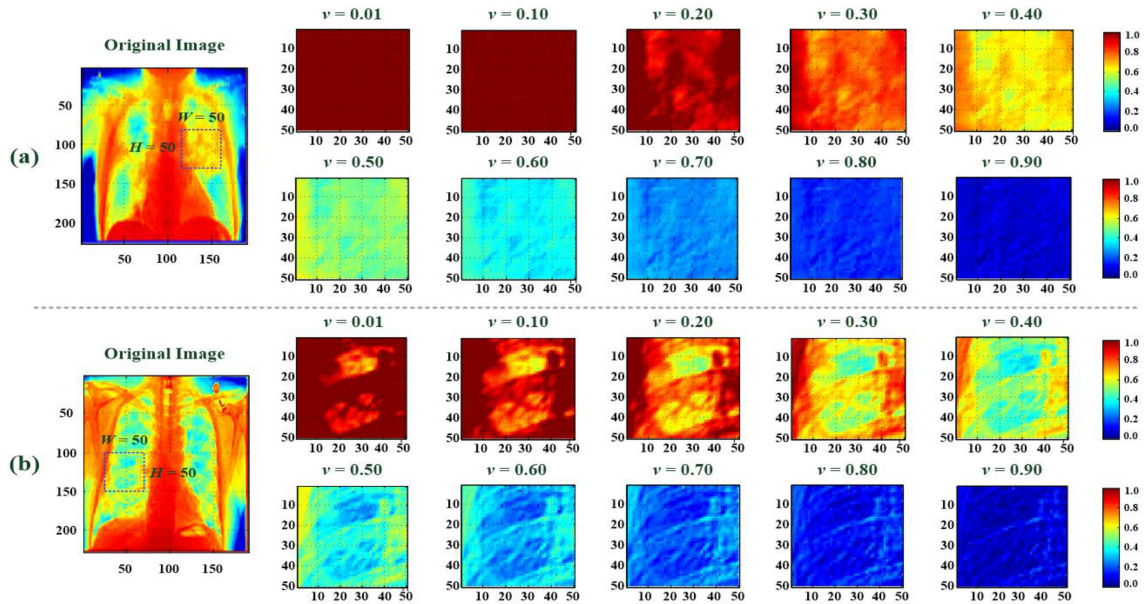
Fig. 8. CXR image enhancement with fractional-order parameters from 0.01 to 0.90. (a) Case study of subject with P, (b) case study of subject with F.

3.1 Multilayer Machine Vision Classifier Training and Testing: A Case Study

In image enhancement, 2D FOC operation in the horizontal and vertical directions was used to enhance the original CXR image within the ROI, as shown by the subject with novel COVID-19 (symptoms: fever and cough). The fractional-order parameter (v) was set to $v = 0.3$ for all CXR images in this study. After digitalized image enhancement, feature pattern involving lesion in matrix form was extracted with a 50×50 B-box, as presented by the right (①) and left (②) feature patterns in Fig. 9(c). Then, we rescaled the feature pattern from $1 \times 2,500$ to 1×625 in vector form using the flattening process, pattern reconstruction, and pooling process. The pattern reconstruction for eight classes could be shown as the vector form (green line) in Fig. 4 or matrix form in Fig. 10. This 1×625 pooling feature pattern was then fed into the inputs of GRA-based classifier. In the learning stage, 223 trained patterns (25 Ns, 34 Pts, 15 Es, 28 Ins, 25 Ms, 46 Ps, 25 Fs, and 25 Efs) were randomly selected from eight labeled classes to train the machine vision classifier, and the 223 remaining feature patterns as untrained patterns were randomly selected to evaluate the performance of the classifier with a K-fold cross-validation at the recalling stage.

As shown in Fig. 6, the structure of GRA-based classifier could be determined with the 223 input–output paired feature patterns, including $\Phi_q = [\phi_1(q), \phi_2(q), \phi_3(q), \cdot, \phi_{625}(q)]$ and $[w_{q1}, w_{q2}, w_{q3}, \cdot, w_{q8}] = [0/1, 0/1, 0/1, \cdot, 0/1]$, $w_{qj} \in [0, 1]$, $q = 1, 2, 3, \ldots, 223$, $j = 1, 2, 3, \ldots, 8$, which are denoted by binary values, "1" or "0", for possible class identification. The 223×625 and 223×8 connecting weighted values were stored in weighting matrixes. Then, the classifier structure could be set by 625 input nodes ($n'=625$) in the input layer, 223 GG functions in a RBN ($Q = 223$), a maximum operation layer, and eight output nodes (eight classes) in the output layer. Parameter RC was $\xi = 5$ in each GG function. The proposed GRA-based classifier was employed to perform the pattern recognition task in a straightforward mathematical operation for numerical and binary data computations without adjusting any of the parameters at the learning stage. For 223 trained patterns as testing patterns, a learning accuracy of 100% was guaranteed to identify the eight classes in the learning stage. The total CPU time was about 4.8787 s.

For a case study, as presented in Figs. 9(a) and 9(b), a subject with COVID-19 had fever and cough (follow-up of 5 days) and revealed worsening of bilateral perihilar and lower region consolidation [41], which were caused by filling of the small airway with fluid (pus or water) or dead
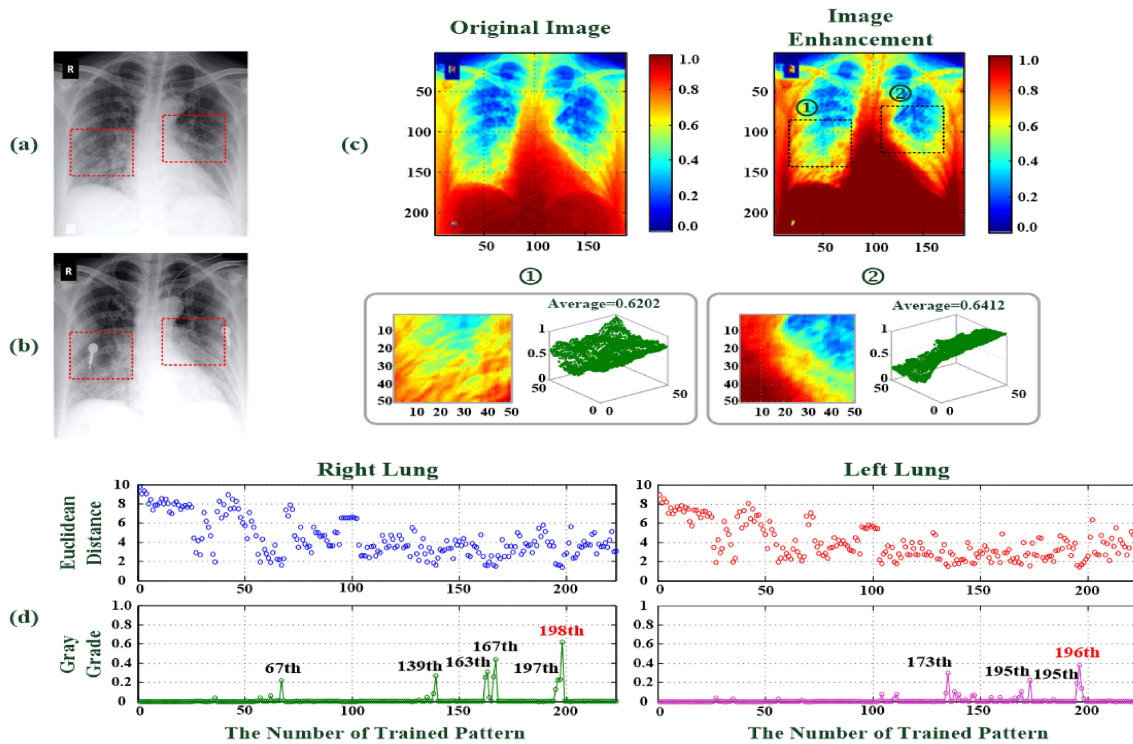
Fig. 9. CXR images of a subject with fever and cough indicating novel COVID-19 [41]. (a) Initial CXR image: bilateral perihilar region consolidation, (b) follow-up CXR image (5 days later): worsening of bilateral perihilar and lower region consolidation, (c) digital image enhancement and bilateral feature patterns, (d) EDs and GGs versus the number of trained patterns for numerical computation results in RL and LL.
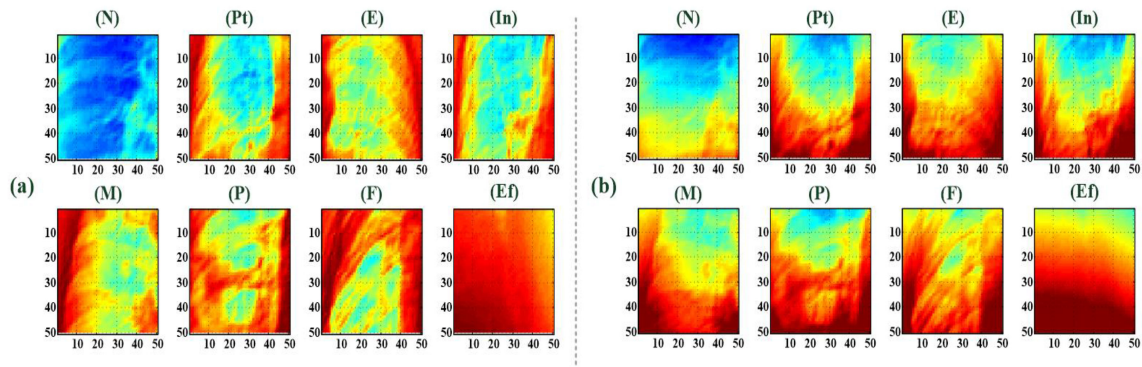
Fig. 10. Feature patterns in matrix form. (a) Original feature patterns for eight classes; (b) restructured feature patterns for eight classes.

white blood cells in bilateral lungs. Consolidation symptoms might cause difficulty in breathing in the subject (shortness of breath). Two untrained feature patterns (pattern ①: mean gray gradient = 0.6202; pattern ②: mean gray gradient = 0.6412) were extracted from the CXR image of the RL and LL (Fig. 9(c)), and these patterns could be fed into the GRA-based classifier to identify the possible classes. In the RBN, with the GG functions, EDs were employed to measure the similarity degree between 2 untrained patterns and 223 trained patterns. The high similarity degree would indicate the minimum ED value and maximum GG value, for example, two untrained patterns

TABLE 2
Experimental Results of 10-Fold Cross Validation for GRA-Based Classifier With 2D FOC and Pattern Reconstruction Processes

Cross Validation	Trained Patterns	Untrained Patterns	Recall (%)	Precision (%)	Accuracy (%)	F1 Score
1			99.42 (TP: 172, FN: 1)	86.87 (TP: 176, FP: 26)	87.89 (27 failures)	0.9272
2	Random Selection	Random Selection	100.00 (TP: 173, FN: 0)	87.92 (TP: 173, FP: 25)	88.79 (25 failures)	0.9326
3	34 Pts, 25 Efs,	34 Pts, 25 Efs,	100.00 (TP: 175, FN: 0)	88.38 (TP: 175, FP: 23)	89.68 (23 failures)	0.9383
4	15 Es, 28 Ins, 25 Ms, 46 Ps,	15 Es, 28 Ins, 25 Ms, 46 Ps,	100.00 (TP: 174, FN: 0)	87.88 (TP: 176, FP: 24)	89.24 (24 failures)	0.9355
5	25 Fs, 25 Ns	25 Fs, 25 Ns	99.42 (TP: 173, FN: 1)	87.37 (TP: 173, FP: 25)	88.34 (26 failures)	0.9301
6	Disease Present:	Disease Present:	99.43 (TP: 175, FN: 1)	88.38 (TP: 175, FP: 23)	89.23 (24 failures)	0.9358
7	198 patterns	198 patterns	100.00 (TP: 174, FN: 0)	87.88 (TP: 174, FP: 24)	89.24 (24 failures)	0.9355
8	Disease Absent: 25 patterns	Disease Absent: 25 patterns	99.43 (TP: 173, FN: 1)	87.37 (TP: 173, FP: 25)	88.34 (26 failures)	0.9301
9	Total of Trained	Total of Trained	99.43 (TP: 175, FN: 1)	88.38 (TP: 175, FP: 23)	89.24 (24 failures)	0.9358
10	Pattern: 223	Pattern: 223	99.43 (TP: 174, FN: 1)	87.88 (TP: 174, FP: 24)	88.79 (25 failures)	0.9330
Average (%)			99.66	87.78	88.88	0.9334

Note: 1) Recall (%)$= \left(\frac{TP}{TP+FN}\right) \times 100\%$, where *TP* and *FN* are the true positive and false negative, respectively.
2) Precision (%)$= \left(\frac{TP}{TP+FP}\right) \times 100\%$, where TP and FP are true positive and false positive, respectively.
3) Accuracy (%)$= \left(\frac{TP+TN}{TP+FN+TN+FP}\right) \times 100\%$, (4) F1 Score$= \frac{2TP}{2TP+FP+FN}$ [47].

were most similar to the #198th and #196th trained patterns within the subdataset of Class #F (Fig. 9(d)). This case was also likely similar to Class #P, as #139th, #163rd, #167th, and #173rd trained patterns within the subdataset of Class #P. Then, the final outputs were computed using Equations (15) to (20):

- outputs in RL: Y = [0.00, 0.00, 0.00, 0.00, 0.00, 0.00, 1.00, 0.00] and $O_7 = 1$ for identifying the Class #F in RL;
- outputs in LL: Y = [0.00, 0.00, 0.00, 0.00, 0.00, 0.00, 1.00, 0.00] and $O_7 = 1$ for identifying the Class #F in LL.

The above screening process required a CPU time of 0.2210 s to identify Class #F for the screening task. In clinical investigation, P is the most common cause of lung consolidation, ground glass opacity (hazy opacity), atelectasis, idiopathic pulmonary fibrosis, and idiopathic interstitial pneumonia, which are usually caused by bacteria, viruses, a novel coronavirus, or gastro-esophageal reflux. In the early stage, lung consolidation and In were the possible symptoms, which might have gradually developed into F symptoms in several days. The findings confirmed that the proposed method could provide promising results for rapidly screening the possible classes and offer the similarity degree to trace the disease progressions from Class #P to Class #F.

3.2 K-Fold Cross-Validation and Comparison With a Traditional Setups

At the recalling stage, the 223 untrained patterns were randomly selected from the remaining datasets: 25Ns, 34 Pts, 15 Es, 28 Ins, 25 Ms, 46 Ps, 25 Fs, and 25 Efs, as seen in Table 2. We evaluated the performance of the GRA-based classifier with 2D FOC and pattern reconstruction process using tenfold cross- validation. The mean recall (%), mean precision (%), mean accuracy (%), and mean F1 score [47] were used as indices to validate the screening performance by using true positive (TP), false positive (FP), and false negative (FN), and were also used for comparing the traditional setups Through experimental tests, a mean recall of 99.66% and a mean precision of 87.78% for identifying the "*disease present* (TP)" and a mean accuracy of 88.88% for determining the possible correct classes (for both "*disease present*" and "*disease absent*") were obtained in tenfold cross-validation as mean mismatches (25) with 1 failure in N, 5 failures in Pt, 3 failures in E, 3 failures in In, 1 failure in M, 5 failures in P, 4 failures in F, and 3 failures in Ef, as seen

TABLE 3
Experimental Results of 10-Fold Cross Validation for GRA-Based Classifier With 2D FOC

Cross Validation	Trained Patterns	Untrained Patterns	Recall (%)	Precision (%)	Accuracy (%)	F1 Score
1			98.82 (TP: 167, FN: 2)	84.34 (TP: 167, FP: 31)	84.06 (33 failures)	0.9101
2	Random Selection	Random Selection	98.81 (TP: 166, FN: 2)	83.84 (TP: 166, FP: 32)	83.57 (34 failures)	0.9071
3	34 Pts, 25 Efs,	34 Pts, 25 Efs,	99.40 (TP: 165, FN: 1)	83.33 (TP: 165, FP: 33)	83.57 (34 failures)	0.9066
4	15 Es, 28 Ins, 25 Ms, 46 Ps,	15 Es, 28 Ins, 25 Ms, 46 Ps,	98.81 (TP: 166, FN: 2)	83.83 (TP: 166, FP: 32)	83.57 (34 failures)	0.9071
5	25 Fs, 25 Ns	25 Fs, 25 Ns	99.39 (TP: 164, FN: 1)	82.83 (TP: 164, FP: 34)	83.09 (35 failures)	0.9036
6	Disease Present: 198 patterns	Disease Present: 198 patterns	98.81 (TP: 166, FN: 2)	83.84 (TP: 166, FP: 32)	83.57 (34 failures)	0.9071
7	Disease Absent:	Disease Absent:	98.80 (TP: 165, FN: 2)	83.33 (TP: 165, FP: 33)	83.09 (35 failures)	0.9041
8	25 patterns	25 patterns	98.81 (TP: 166, FN: 2)	83.84 (TP: 166, FP: 32)	83.57 (34 failures)	0.9071
9	Total of Trained Pattern: 223	Total of Trained Pattern: 223	99.39 (TP: 162, FN: 1)	81.82 (TP: 162, FP: 36)	82.13 (37 failures)	0.8975
10			98.82 (TP: 168, FN: 2)	84.85 (TP: 168, FP: 30)	84.54 (32 failures)	0.9130
Average (%)			98.98	83.59	83.48	0.9063

experimental results in Table 2. A mean precision of 87.78% was greater than 80.00%, as a positive predictive value (PPV), to evaluate the performance of the proposed classifier. The recall(%) as the sensitivity (mean TP: 174, mean FN: 1) was a higher index to identify the possible TP in 7 major lung diseases. The mean F1 score = 0.9334 also indicated a high value to evaluate the performance of the proposed GRA-based classifier, which could provide promising results for rapid screening.

In addition, the 2D FOC process, maximum pooling process, flattening processes, and a GRA-based classifier [27] could also be integrated into a multilayer machine vision classifier. The extracted feature patterns were of size 50×50, we also flattened and pooled them from 50×50 to 1×625. Hence, the same structure of GRA-based classifier was setup. With tenfold cross-validation using the same datasets as seen in Table 3, a mean recall of 98.99%, a mean precision of 83.59%, a mean accuracy of 83.48%, and a mean F1 score of 0.9063 were obtained as mean mismatches (35) with 2 failures in N, 6 failures in Pt, 3 failures in E, 4 failures in In, 4 failures in M, 6 failures in P, 6 failures in F, and 4 failures in Ef. These experimental results were presented in Table 3. PPV was also greater than 80.00% for identifying the possible "*disease present* (TP)." In contrast to the GRA-based classifier with 2D FOC process, the experimental results indicated that the proposed classifier had higher mean recall, mean precision, and mean accuracy in the clinical indication. The proposed classifier also had a higher mean F1 score (0.9334) than one (0.9063) of the GRA-based classifier without pattern reconstruction process for measuring the harmonic mean of recall and precision indexes, and also improved the screening accuracy from 83.48% (mean 2 mismatches in TN and 33 mismatches in TP) to 88.88% (mean 1 mismatch in TN and 24 mismatches in TP) for identifying the TP and TN cases among the total number untrained patterns.

The experimental tests showed that the proposed method performed better than the GRA-based classifier with 2D FOC in terms of PPV and accuracy for screening subjects with single or multiple symptoms. However, the CXR scans in A-P views were restricted by their low contrast, medium quality, and lack of three-dimensional (3D) information for indicating details in the chest cavity. In a case study, a subject (male, aged 83 years, with hypertension and Type 2 diabetes mellitus [41]) was diagnosed with COVID-19 pneumonia with fever (38.9 °C) and cough. The TP result was confirmed by PCR examination. After digital image enhancement with 2D FOC operation, lung consolidation and pulmonary emphysema were found in the right middle, right lower, and left middle lobes, as indicated by the red B-boxes in Fig. 11(a). Then, two feature patterns (bilateral mean gray gradients = 0.4463 and 0.5477) were extracted and fed into the GRA-based classifier to identify the possible classes. As presented in Fig. 11(c), with the GG functions in the RBN, the EDs were employed to measure the similarity degree between 2 feature patterns and 223 trained feature patterns. The minimum ED value and high similarity degree were associated with the 49th and 76th
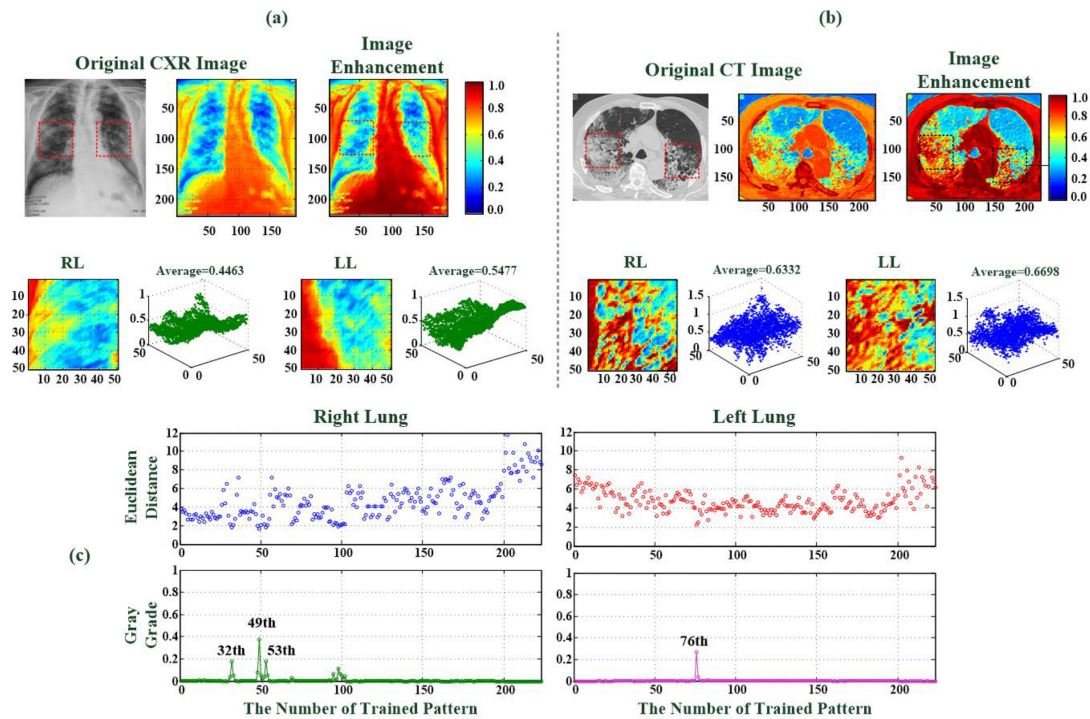
Fig. 11. CXR and CT imaging scans for a subject with novel COVID-19 P [40]. (a) Original CXR film, image enhancement, and feature patterns for bilateral lungs; (b) original CT film, image enhancement, and feature patterns for bilateral lungs; (c) EDs and GGs versus the number of trained patterns for numerical computation results in RL and LL.

patterns in the RL and LL, respectively. The GRA-based classifier identified classes #Pt and #In and established In risk to continuously provide notice of disease progression. With CT imaging examination (Fig. 11(b)), we observed multiple ground glass opacities as initial consolidation phenomena (segmental consolidation), resulting in the risk of acute pulmonary embolism. In taking CT imaging scans, a computer can be used to obtain the cross-sectional films of internal structures that could clearly indicate the extent of lung damage caused by consolidation, In, or F. Such films can help narrow down the diagnosis and guide decisions for follow-up treatment and analysis. With 3D information, CT imaging could make internal structures, such as tumors, lung, heart, and blood vessels in the chest cavity, increasingly apparent, thereby allowing radiologists and physicians to identify the locations, textures, shapes, densities, and sizes of lesions. CT images could also be enhanced by increasing the sharpness and brightness of specific features (bilateral mean gray gradients = 0.6332 and 0.6698) via the 2D FOC operation (Fig. 11(b)). Such imaging could also facilitate the examination of abnormalities found in A-P CXR images. In clinical applications, CXR imaging serves as a primary diagnostic method for assessing lung diseases. Hence, radiologists and physicians could use the proposed screening method with CXR images to rapidly assess medical conditions and achieve early disease detection.

4. Conclusion

In this study, a multilayer fractional-order machine learning classifier had been used to rapidly screen any lung lesion in bilateral lung zones. The screening process consisted of a 2D FOC process, a flattening process, a pattern reconstruction with IFS, a pooling process, and a GRA-based classifier. For 2D FOC process, the fractional-order parameter $v = 0.3$ was selected for all enrolled

CXR images to enhance possible lesions in specific B-boxes (50 × 50 pixel) from low contrast CXR films. Then, IFS with NIFs was used to restructure the feature patterns, which made the feature patterns more distinguishable for further pattern recognition. The quantitative restructured patterns were positively correlated with the classes of lung diseases. After digitalized image processes, the bilateral feature patterns (right / left lung) were fed to the GRA-based classifier, which could identify the possible class and display the similarity degree for assessing causes and diseases progress. Through 10-fold cross-validation, the feasibility of the proposed multilayer classifier, relative to the GRA-based classifier with 2D FOC, was validated and evaluated with a mean recall of 99.66%, a mean precision of 87.78%, a mean accuracy of 88.88%, and a mean F1 score of 0.9334 and a mean of 25 mismatches in TP and TN cases. All score indexes of the proposed classifier were higher than those of traditional setups for TP case identification. Hence, for the feature patterns fed with 2D FOC and IFS processes, the GRA-based classifier could improve the accuracy rate from 83.48% to 88.88% to separate "*disease present*" from "*disease absent*" and enable clinicians to respond for treatment actions. In clinical applications, new case studies could be continually mined from clinical investigations, and new CXR images of these cases could be analyzed and appraised by clinicians and radiologists to achieve continuous data collection for retraining the classifier. The proposed GRA-based classifier could adapt itself by using adding real world feature patterns in the RBN without parameter assignments, statistical methods, and complex iteration computations. For further CADM development and to address the bottleneck in CXR, GRA-based classifier could also train new medical images, such as CT imaging or high resolution magnetic resonance imaging, to enhance screening functions which could raise the accuracy rate and keep the intended medical purpose in medical devices or commercial off-the-shelf platforms for further clinical applications.

References

[1] T.-Y. D. Cheng, S. M. Cramb, P. D. Baade, D. R. Youlden, C. Nwogu, and M. E. Reid, "The international epidemiology of lung cancer: Latest trends, disparities, and tumor characteristics, "*J. Thoracic Onco.*, vol. 11, no. 10, pp. 1653–1671, 2016.

[2] D. Planchard and B. Besse, "Lung cancer in never-smokers," *Eur. Respiratory J.*, vol. 45, pp. 1214–1217, 2015.

[3] S. Teramoto, T. Ishil, H. Yamamoto, Y. Yamaguchi, and Y. Ouchi, "Nasogastric tube feeding is a cause of aspiration pneumonia in ventilated patients," *Eur. Respiratory J.*, vol. 27, no. 2, pp. 436–437, 2006.

[4] I. Sirazitdinov, M. Kholiavchenko, T. Mustafaev, Y. Yixuan, R. Kuleev, and B. Ibragimov, "Deep neural network ensemble for pneumonia localization from a large-scale chest x-ray database," *Comput. Elect. Eng.*, vol. 78, pp. 388–399, 2019.

[5] W.-H. Huang *et al.*, "2019 novel coronavirus disease (COVID-19) in Taiwan: reports of two cases from Wuhan, Chia," *J. Microbio., Immuno. Infection*, vol. 53, pp. 481–484, 2020.

[6] S. Tian, W. Hu, L. Niu, H. Liu, H. Xu, and S.-Y. Xiao, "Pulmonary pathology of early-phase 2019 Novel Coronavirus (COVID-19) pneumonia in two patients with lung cancer," *J. Thoracic Onco.*, vol. 15, pp. 700–704, 2020.

[7] L. L. Thomala, "Pneumonia mortality rate in Taiwan 2018, by gender," 2019, [Online]. Available: https://www.statista.com/statistics/ 1079651/taiwan-pneumonia-death-rate-gender/

[8] B. S. Kancherla, M. K. Dishop, S. S. Rothenberg, and L. L. Fan, "Diffuse pulmonary infiltrates in an immunocompromised patient," *J. Allergy Clin. Immuno.*, vol. 121, no. 2, pp. 540–542, Feb. 2008.

[9] P.-Y. Chen, C.-H. Lin, C.-D. Kan, N.-S. Pai, W.-L. Chen, and C.-H. Li, "Smart pleural effusion drainage monitoring system establishment for rapid effusion volume estimation and safety confirmation," *IEEE Access*, vol. 7, pp. 135192–135203, 2019.

[10] C.-H. Lin, C.-D. Kan, W.-L. Chen, and P.-T. Huang, "Application of two-dimensional fractional-order convolution and bounding box pixel analysis for rapid screening of pleural effusion," *J. X-Ray Sci. Technol.*, vol. 27, no. 3, 2019, pp. 517–535.

[11] National Institute of Environmental Health Sciences (NIH), Lung Diseases, 2020, [Online]. Available: https://niehs.nih.gov/health/topics/ Conditions/lung-disease/index.cfm#footnote1

[12] J. Marx, *Rosen's Emergency Medicine: Concepts and Clinical Practice*, 7th Ed., Philadelphia, PA, USA: Mosby/Elsevier, 2010, pp. 393–396.

[13] M. P. Moy, J. M. Levsky, N. S. Berko, A. Godelman, V. R. Jain, and L .B. Haramati, "A new, simple method for estimating pleural effusion size on CT scans," *Chest*, vol. 143, no. 4, pp. 1054–1059, 2013.

[14] H. M. Zaeim, C. Scheffer, M. Blanckenberg, and K. Dellimore, "Evaluation of the use of frequency response in the diagnosis of pleural effusion on a phantom model of the human lungs," in *Proc. 2014 36th Annu. Int. Conf. IEEE Eng. Med. Biol. Soc.*, 2014, pp. 3418–3421.

[15] S. Ahdi Rezaeieh and A. M. Abbosh, "Review of systems for the detection and monitoring of accumulated fluids in the human torso," in *Proc. Int. Symp. Antennas Propag.*, 2015, pp. 1–4.

[16] X. Wang, Y. Peng, L. Lu, Z. Lu, M. Bagheri, and R. M. Summers, ChestX-ray8: Hospital-scale chest X-ray database and benchmarks on weakly-supervised classification and localization of common thorax diseases, in *Proc. IEEE CVPR*, 2017, pp. 2097–2106.

[17] M. Arsalan, M. Owais, T. Mahmood, J. Choi, and K. R. Park, "Artificial intelligence-based diagnosis of cardiac and related diseases," *J. Clin. Medicine*, vol. 9, no. 871, pp. 1–25, 2020.

[18] H. Wang, H. Jia, L. Lu, and Y. Xia, "Thorax-net: an attention regularized deep neural network for classification of thoracic disease on chest radiography," *IEEE J. Biomed. Health Informat.*, vol. 24, no. 2, pp. 475–485, Feb. 2020.

[19] Y.-F. Pu, J.-L. Zhou, and X. Yuan, "Fractional differential mask: a fractional differential-based approach for multiscale texture enhancement," *IEEE Trans. Image Process.*. vol. 19, no. 2, pp. 491–511, Feb. 2010.

[20] P.-Y. Chen, C.-H. Lin, C.-D. Kan, N.-S. Pai, W.-L. Chen, and C.-H. Li, "Smart pleural effusion drainage monitoring system establishment for rapid effusion volume estimation and safety confirmation," *IEEE Access*, vol. 7, pp. 135192–135203, 2019.

[21] T. Lindeberg, E. Detection, H. Michiel (Ed.), *Encyclopedia of Mathematics, Springer Science*, Business Media B.V./Kluwer Academic Publishers, 2001.

[22] M. Barnsley, *Fractals Everywhere*, 2nd Edition, San Francisco, CA, USA: Academic Press, Elsevier Inc., 1993, ISBN 978-0-12-079061-6.

[23] J. J. van Wijk and D. Saupe, "Image based rendering of iterated function systems," *Comput. Graph.*, vol. 9, pp. 1–17, 2004.

[24] C.-H. Lin and Yi-C Du, "Fractal QRS-complexes pattern recognition for imperative cardiac arrhythmias," *Digit. Signal Process.*, vol. 20, pp. 1274–1285, 2010.

[25] P. Y. Ktonas, S. Gatzonis, H. Tsekou, and D. Sakas, "Comparison of fractal dimension estimation algorithm for epileptic seizure onset detection," *J. Neural Eng.*, vol. 7, pp. 1–18, 2010.

[26] K. C. Chang and M. F. Yeh, "Grey relational analysis based approach for data clustering," *IEE Proc.-Vision Image Signal Process.*, vol. 152, no. 2, pp. 165–172, 2005.

[27] C.-H. Lin, "Frequency-domain features for ECG beat discrimination using grey relational analysis-based classifier," *Comput. Math. Appl.*, vol. 55, no. 4, pp. 680–690, 2008.

[28] Y. Wua, F. Zhou, and J. Kong, "Innovative design approach for product design based on TRIZ, AD, fuzzy and Grey relational analysis," *Comput. Ind. Eng.*, vol. 140, pp. 1–12, 2020.

[29] F. Sarrafa and S. H. Nejadb, "Improving performance evaluation based on balanced scorecard with grey relational analysis and data envelopment analysis approaches: Case study in water and wastewater companies," *Eval. Program Planning*, vol. 79, pp. 1–12, 2020.

[30] Nation Institutes of Health (NIH), Clinical Center, Images are Available via Box, 2019, [Online], Available: https://Nihcc.app.box.com/v /ChestXray-NIHCC

[31] D. Chicco and G. Jurman, "The advantages of the Matthews correlation coefficient (MCC) over F1 score and accuracy in binary classification evaluation," *BMC Genomics*, vol. 21, no. 6, pp. 1–13, 2020.

[32] Y. Shao, Y. Gao, Y. Guo, Y. Shi, X. Yang, and D. Shen, "Hierarchical lung field segmentation with joint shape and appearance sparse learning," *IEEE Trans. Med. Imag.*, vol. 33, no. 9, pp. 1761–80, Sep. 2014.

[33] B. Ibragimov, B. Likar, and F. Pernus, "A game-theoretic framework for landmark-based image segmentation," *IEEE Trans. Med. Imag.*, vol. 31, no. 9, pp. 1761–1776, Sep. 2012.

[34] Y. Shi *et al.*, "Segmenting lung fields in serial chest radiographs using both populationbased and patient-specific shape statistics," *IEEE Trans. Med. Imag.*, vol. 27, no. 4, pp. 481–494, Apr. 2008.

[35] S. Vajda *et al.*, "Feature selection for automatic tuberculosis screening in frontal chest radiographs," *J. Med. Syst.*, vol. 42, no. 146, pp. 1–11, 2018.

[36] K. C. Santosh and S. Antani, "Automated chest X-ray screening: Can lung region symmetry help detect pulmonary abnormalities?" *IEEE Trans. Med. Imag.*, vol. 37, no. 5, pp. 1168–1177, May 2018.

[37] P. J. Rajpurkar *et al.*, "Chexnet: radiologist-level pneumonia detection on chest x-rays with deep learning," 2017, *arXiv: 1711.05225*.

[38] B. Ibragimov, D. Toesca, D. Chang, Y. Yuan, A. Koong, and L. Xing, "Development of deep neural network for individualized hepatobiliary toxicity prediction after liver SBRT," *Med. Phys.* vol. 45, no. 10, pp. 4763–4774, 2018.

[39] Y. C. Lin *et al.*, " Deep learning for fully automated tumor segmentation and extraction of magnetic resonance radiomics features in cervical cancer," *Eur. Radiol.*, vol. 30, no. 3, pp. 1297–1305, 2019.

[40] K. C. Santosh, "AI-driven tools for coronavirus out outbreak: need of active learning and cross-population train / test models on multitudinal / multimodal data," *J. Med. Syst.*, vol. 44, no. 93, pp. 1–5, 2020.

[41] J. P. Cohen, P. Morrison, and L. Dao, ieee8023/covid-chestxray-dataset, 2020, *arXiv:2003.11597*, [Online]. Available: https://github.com/ieee8023/covid-chestxray-dataset/tree/master/ images

[42] J. B. Reece, L. A. Urry, M. L. Cain, S. A. Wasserman, P. V. Minorsky, and R. B. Jackson, *Amplifying DNA: The Polymerase Chain Reaction (PCR) and Its Use in DNA Cloning*, 10th ED., San Francisco, CA, USA: Pearson, 2011.

[43] J. B. Reece, M. R. Taylor, E. J. Simon, and J. L. Dickey, DNA profiling in Campbell biology: concepts & connections, 7th ED., 2012.

[44] N.-Y. Lee *et al.*, "A case of COVID-19 and pneumonia returning from Macau in Taiwan: Clinical course and anti-SARS-coV-2 IgG dynamic," *J. Microbio., Immunol. Infection*, vol. 53, pp. 485–487, Mar. 2020.

[45] S A. Bustin, "How to speed up the polymerase chain reaction," *Biomol. Detect. Quantif.*, vol. 12, pp. 10–14, 2017.

[46] C. Huang *et al.*, "Clinical features of patients infected with 2019 Novel Coronavirus in Wuhan, China," *The Lancet*, vol. 395, no. 10223, pp. 497–506, 2020.

[47] D. Chicco and G. Jurman, "The advantages of the Matthews correlation coefficient (MCC) over F1 score and accuracy in binary classification evaluation," *BMC Genomics*, vol. 21, no. 6, pp. 1–13, 2020.

[48] U. Bagci, M. Bray, J. Caban, J. Yao, and D. J. Mollura, "Computer-assisted detection of infectious lung diseases: A review," *Comput. Med. Imag. Graph.*, vol. 36, no. 1, pp. 72–84, 2012.